Application of catalysts in the synthesis of 4-(4-(dimethylamino) benzylidene)-3-methylisoxazol-5(4H)-one: experimental and theoretical studies

Shazalia Mahmoud Ahmed Ali[1] · Amani Chrouda[1] · Manahil Babiker Elamin[1] · Ibrahim S. Yahia[2,3,4] · Heba Y. Zahran[2,3,4] · Samer H. Zyoud[5]

Abstract

The aim of this work is to evaluate the catalytic activity of catalysts based on silver nanoparticles in the synthesis of isoxazolone-type heterocycles. The catalysts used in this study were prepared by the impregnation of 2 wt% Ag on commercial support oxides which are: Al_2O_3, CeO_2 and MgO. The characteristics of these materials are obtained using the following methods: inductively coupled plasma atomic emission spectroscopy (ICP), X-ray diffraction (XRD), Fourier transform infrared (FTIR) spectroscopy, Raman spectroscopy, adsorption–desorption of N_2 and Diffuse reflectance UV–visible (RD/UV–Vis). The results of the application of the catalysts $Ag–Al_2O_3$, Ag–MgO and $Ag–CeO_2$ in the synthesis of the 4-(4-(dimethylamino) benzylidene)-3-methylisoxazol-5(4H)-one using an aldehyde as the starting molecule, were revealed that all the catalysts had interested yields up to 60%. However, the $Ag–CeO_2$ catalyst showed a yield that goes to 94% respecting the rules of green chemistry. On the other hand, it turned out that the reaction does not work using a ketone as the starting molecule whatever the reaction conditions. Finally, the study was closed by a theoretical study of the properties of the molecule obtained.

✉ Shazalia Mahmoud Ahmed Ali
m.elamn@mu.edu.sa

✉ Amani Chrouda
amanichrouda5@gmail.com

1 Department of Chemistry, College of Science Al-Zulfi, Majmaah University, P.O. Box 11952, Al Majmaah, Saudi Arabia

2 Laboratory of Nano-Smart Materials for Science and Technology (LNSMST), Department of Physics, Faculty of Science, King Khalid University, P.O. Box 9004, Abha, Saudi Arabia

3 Research Center for Advanced Materials Science (RCAMS), King Khalid University, P.O. Box 9004, Abha 61413, Saudi Arabia

4 Nanoscience Laboratory for Environmental and Biomedical Applications (NLEBA), Semiconductor Lab, Department of Physics, Faculty of Education, Ain Shams University, Roxy 11757, Cairo, Egypt

5 Nonlinear Dynamics Research Center (NDRC), Department of Mathematics and Sciences, Ajman University, Ajman, United Arab Emirates

1 Introduction

Five-member cyclic oxime esters, comprising at the same time oxygen and nitrogen atoms, also known as isoxazolones or more precisely 4H-isoxazol-5-ones, have attracted a lot of attention recently thanks to their applications in the pharmacological field as antibacterial, anticonvulsant, antifungal, antidiabetic, anticancer and also used as fungicides and insecticides in agro-chemistry [1]. Several methods have been developed to achieve the structure of the 4H-isoxazol-5-ones derivatives. Recently, homogenous or heterogeneous catalysts have been applied in the three-component condensation of β-oxoesters, hydroxylamine hydrochloride and aromatic aldehydes [1–7]. As shown in Table 1, homogenous catalysts lead to higher yields but cannot be recovered and reused at the reaction end. However, nanomaterials have several advantages and are often used in organic synthesis [8–12]. The use of heterogeneous catalysts in organic synthesis is a variant that is becoming increasingly interesting because of the advantages it presents: i) easy separation of the catalyst from the reaction mixture, ii) simplified recovery and catalyst recycling,

Table 1 Optimal conditions cited in the literature for the synthesis of α,β-unsaturated isoxazol-5(4H)-ones

Products	Conditions	Yields (%)	References
3-Methyl-4-arylmethylene-isoxazol-5(4H)-ones derivative of 4-hydroxybenzaldehyde	Time: 30 min; temperature: 70 °C; solvent: H_2O; catalyst: 12 mmol% of [H-Pyrr][H_2PO_4]	97	[6]
	Time: 130 min; room temperature; solvent: H_2O; catalyst: 10 mmol% of potassium phthalimide	95	[5]
3,4-Disubstituted Isoxazole-5(4H)-ones	Time: 75 min; room temperature; Solvent: H_2O; catalyst: 10 mmol% of Ni(OAc)$_2$.H_2O	95	[15]
(Z)-4-(3-hydroxybenzylidene)-3-methylisoxazol-5(4H)-one	Time: 120 min; room temperature; solvent: H_2O; catalyst: 0.07 g of SbCl$_3$	90	[7]
3,4-Disubstituted isoxazol-5(4H)-one	Time: 30 min; temperature: 70 °C; Solvent: H_2O; catalyst: 0.005 g of ZnO@Fe$_3$O$_4$	93	[14]
α,β-Unsaturated isoxazol-5(4H)-ones	Time: 30 min; temperature: 70 °C; solvent: H_2O; catalyst: 0.05 g of nano-SiO$_2$–H_2SO_4	90	[16]
Isoxazol-5(4H)-one derivatives	Time: 3 min; temperature: 60 °C; solvent: H_2O; catalyst: 0.03 g of 6-methylguanamine–CoFe$_2$O$_4$	94	[17]
	Time: 3 min; temperature: 60 °C; solvent: H_2O; without catalyst	No reaction	
	Time: 3 min; room temperature; solvent: H_2O; catalyst: 0.03 g of 6-methylguanamine–CoFe$_2$O$_4$	Trace	
	Time: 60 min; room temperature; Solvent: H_2O; catalyst: 0.03 g of Ag/SiO$_2$	93	[2]
3-Methyl-4-(1-phenylmethylene)-5-isoxazolone	Time: 60 min; room temperature; solvent: H_2O; catalyst: 15% mmol of GuHCl	90	[18]
3-Methyl-4-arylmethylene-isoxazol-5(4H)-ones	Time: 2.5 h; room temperature; solvent: EtOH; catalyst: 5 mmol% Na$_2$S.9H_2O	80	[19]
4-(3-Hydroxybenzylidene)-3-methylisoxazol-5(4H)-one	Time: 55 min; temperature:90 °C; solvent: H_2O:EtOH (9:1); catalyst: 1 mL citrus lemon (lemon juice)	94	[20]
Isoxazol-5(4H)-ones derivatives	Time: 3 h; room temperature; solvent: EtOH; catalyst: 0.04 g of Au–Fe/ZrO$_2$	78	[4]
(Z)-4-(4-methylbenzylidene)-3-methylisoxazol-5(4H)-one	Room temperature; solvent: EtOH; catalyst: 0.05 g of 5%Ag/Bentonite	89	[3]

iii) long catalytic life, iv) saving atoms, v) environment respect [13], vi) helps to diminish cost-effectiveness, and vii) energy [14]. N. Ameur et al. studied catalysts based on silver nanoparticles for the synthesis of Isoxazol-5(4H)-one derivative [3]. The authors varied the supports (titanate nanotubes and natural Bentonite) and the silver contents (0.5; 2 and 5 wt%). The best activity (around 89%) was purchased in the presence of the 5%Ag/Bentonite catalyst and this was attributed to the large surface area of the catalyst and to the suitable size of the silver nanoparticles (of the order of 2 nm). In a more recent work, the same team applied bimetallic catalysts Au–Fe deposited on TiO$_2$ and ZrO$_2$ in the synthesis of heterocyclic molecules. The best yield (about 78%) was completed in the case of the Au–Fe/ZrO$_2$ catalyst [4]. The literature evoked the application of pyrrolidinium dihydrogen phosphate as a novel catalyst used as efficient catalyst for the synthesis of 3-methyl-4-arylmethylene-isoxazole-5(4H)-ones [6]. In the others hand, the synthesis of isoxazol-5(4H)-one derivatives has been developed using a ZnO@Fe$_3$O$_4$ core–shell catalyst [14]. This multi-compound reaction was carried out in presence

of catalyst and water as solvent. Authors were attributed the high activity of the catalyst to its high selectivity, interesting catalytic activity, simple recovery and high stability. In addition, the application does not necessitate any organic solvent, dangerous metal catalysts, elevated temperatures and may be tolerate a large range of substituent's with different electronic and steric characteristics [14].

The purpose of our study is the study and the application of novel catalysts based on silver nanoparticles in the synthesis of 4-(4-(dimethylamino)benzylidene)-3-methyl-isoxazol-5(4H)-one. It is important for us to develop a new inexpensive, fast and efficient green catalytic protocol under mild reaction conditions, as shown in Fig. 1.

2 Experimental section

2.1 Materials

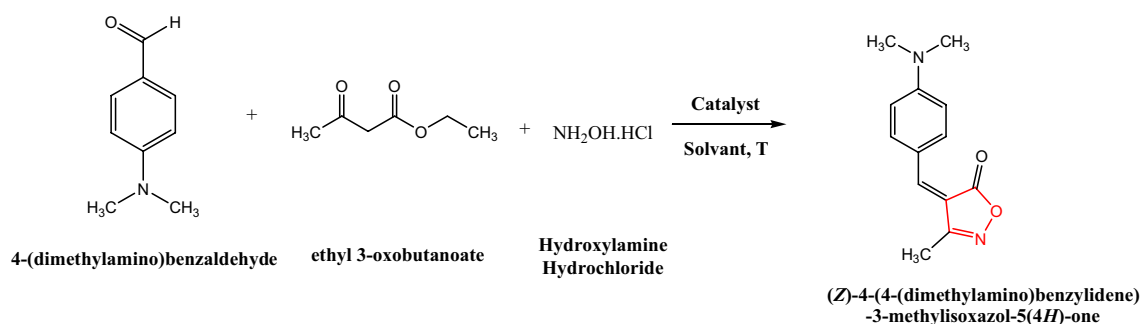All reagents are provided from Sigma-Aldrich and are: aluminum oxide (Alumina, Al$_2$O$_3$, M = 101.96 g.mol^{-1}),

Fig. 1 Synthesis of 4-(4-(dimethylamino)benzylidene)-3-methylisoxazol-5(4*H*)-one using catalysts

Acetoacetic ester($CH_3COCH_2COOC_2H_5$, M = 130.14 g. mol^{-1}), Cerium(IV) oxide (ceria, CeO_2, M = 172.11 g. mol^{-1}), Hydroxylammonium chloride ($NH_2OH \cdot HCl$, M = 69.49 g.mol^{-1}), 4-(Dimethylamino)benzaldehyde, Magnesium Oxide (MgO, M = 40.30 g.mol^{-1}), 4-(Dimethylamino)benzaldehyde (4-[$(CH_3)_2$ N]C_6H_4CHO, M = 149.19 g. mol^{-1}),1-[4-(Dimethylamino)phenyl]ethenone ($C_{10}H_{13}NO$, M = 163.22 g.mol^{-1}),Silver nitrate ($AgNO_3$, M = 169.87 g. mol^{-1}).

2.2 Preparation of nanopowders

The catalysts based on the silver nanoparticles are prepared by incipient wetness impregnation at 2 wt% of silver according to the protocol described in the references [21, 22]. Briefly, the aqueous solution containing the appropriate

mass of silver nitrates is brought into contact with the support for 4 h under stirring in the dark. The mixture is subsequently dried overnight at 120 °C. Finally, the obtained catalysts are annealed at 300 °C under controlled air (N_2/O_2: 80/20) for 4 h. The used catalysts in this study are named: Ag–Al_2O_3, Ag–CeO_2 and Ag–MgO.

2.3 Characterization methods

The studied catalysts were characterized using XRD, ICP, N_2 adsorption–desorption, FTIR and Raman spectroscopy. The amounts of Ag in the catalysts were measured by ICP chemical analysis. FTIR spectra were recorded on an 8400S Shimadzu Spectrophotometer using KBr disks. The structure of materials was determinate using X-ray diffractometer (XRD, Bruker AXS D8-Advanced diffractometer) at a

Fig. 2 NMR^{1}H spectrum of 4-(4-(dimethylamino) benzylidene)-3-methylisoxazol-5(4*H*)-oneproduct
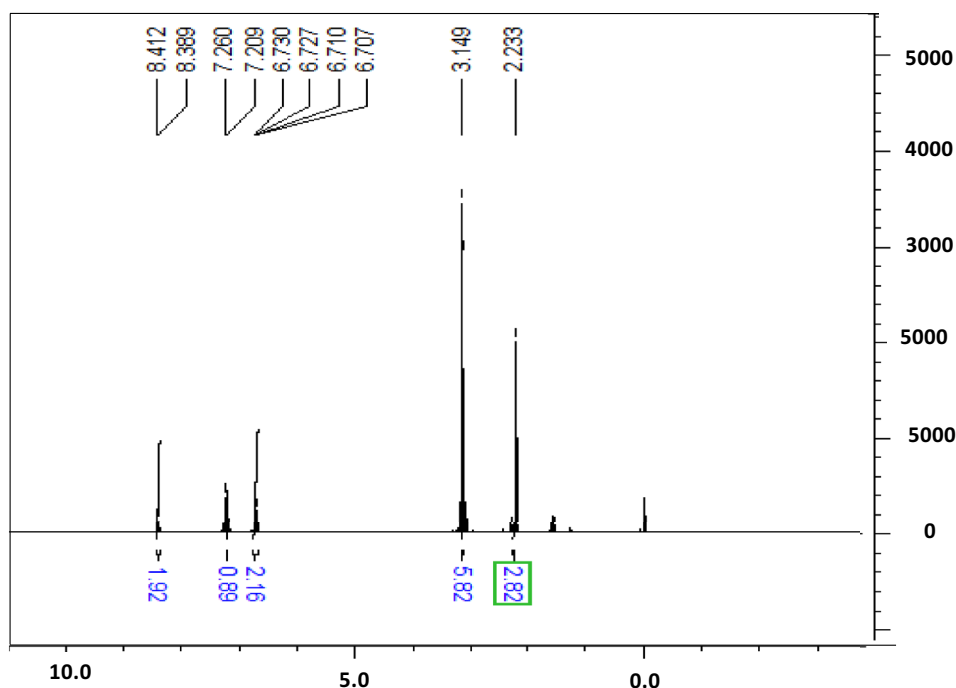
Table 2 Textural and structural proprieties of the studied materials

Catalysts	Crystal-lites' size (nm)	S_{BET} (m².g⁻¹)	Pore size (nm)	Pore volume (cc. g⁻¹)
Al_2O_3	73.6	03.50	88.11	0.15
CeO_2	8.6	83.94	08.16	0.21
MgO	9.7	80.29	14.76	0.38
Ag/Al_2O_3	73.8	06.97	116.52	0.15
Ag/CeO_2	8.6	107.50	09.17	0.22
Ag/MgO	9.6	105.59	31.25	0.38

Table 3 Effect of the catalyst on the synthesis reaction of 3-methyl-4-(4-(Dimethylamino)benzalidene)-isoxazole-5(4H)-one

Entry	Catalysts	Ag(wt%)	TOF (min⁻¹)*10⁺²	Yields (%)
1	Ag/CeO_2	1.8	2.0	94
2	CeO_2	/	1.8	87
3	Ag/Al_2O_3	1.5	1.7	80
4	Al_2O_3	/	1.4	65
5	Ag/MgO	1.8	1.3	64
6	MgO	/	1.2	56

scanning rate of 0.04°/6 s in the 2θ range of 20−80°. The average crystalline size of the product was calculated by the Scherer's equation:

$$d = \frac{k * \lambda}{\beta * cos\theta} \quad (1)$$

where

d is particle size of the crystal, *k* is Scherer's constant (0.9), λ is X-ray wavelength (Cu source, 0.15406 nm), β is the width of the XRD peak at the half height and θ is the Bragg's diffraction angle.

The Raman measurements were determinate by Raman spectrometer LabRam Infinity. The excitation wavelength of 785 nm was chosen for Raman measurements. The BET surface areas were determined by N_2 adsorption–desorption using a Micromeritics Gemini 2360 instrument. Previous to analysis, the catalysts were oven dried at 250 °C for 12 h. Melting point of the resulting heterocyclic molecule was measured on a Buchi 510 melting point apparatus. ^{1}H NMR and ^{13}C NMR of the final heterocyclic molecule spectra were recorded at ambient temperature on a BRUKER AVANCE DRX-400 MHz spectrophotometer using CDCl₃ as the solvent. Diffuse reflectance UV–visible (RD/UV–Vis) spectra of the catalysts were realized using a CARY 5000 (UV–Vis–NIR) spectrophotometer.

2.4 Synthesis of heterocyclic molecules using prepared catalysts

The synthesis of 3-methyl-4-(1-phenylethylidene)-isoxazole-5(4H)-one is carried out by a mixture of aromatic aldehyde or ketone (1.3 g), ethyl acetoacetate (1.3 g) and hydroxylamine hydrochloride (0.7 g)in the presence of 5 mL of solvent (distilled water, ethanol or a mixture of them) and the catalyst (0.02 g) in a flask immersed in a sand bath at different temperature (room temperature and 60 °C). Then, the mixture is left under vigorous stirringfor24 h. It is noted that the reaction with 4-dimethylaminoacetophenone under these conditions did not lead to the formation of the product.

The turnover and yield of the reaction are calculated as follows:

$$Yield(\%) = 100 * \left(\frac{n_0 - n_f}{n_0} \right) \quad (2)$$

$$TOF(min^{-1}) = \frac{n_0 - n_1}{time(min) * \text{mass of the catalyst(g)}} \quad (3)$$

where n_0 and are n_1 the initial and the final mole number (mol), respectively.

Spectral data (NMR) of 4-(4-(dimethylamino) benzylidene)-3-methylisoxazol-5(4H)-one, red solid, melting point: 130–131 °C.

^{1}H NMR (400 MHz, CDCl₃): δ 2.23 (s, 3H), 3.15 (s, 6H), 6.70–6.73 (dd, 1.2 Hz, 2H), 7.20 (s, 1H), 8.39–8.41 (d, J = 8 Hz, 2H) (Fig. 2).

2.5 Computational details

The density functional theory (DFT) [23–27] is currently the most widely used in the study of structure and reactivity of molecular systems [28–30]. In this work, all quantum chemical calculations were carried out using the GAUSSIAN09 software package [31] and Gauss view 5.08 molecular visualization program [32]. The B3LYP hybrid functional [33–35] was used for the geometry optimization in the gas phase. The calculations were performed using the 6-31G(d) basis set. The global properties such as the electronic chemical potential μ [36, 37], the chemical hardness η [36, 38] and the chemical softness S [36] were obtained in terms of the electron energies of the frontier molecular orbitals HOMO (highest occupied molecular orbital) and LUMO (lowest unoccupied molecular orbital), at the ground state using the following equations:

$$\mu = \frac{E_{HOMO} + E_{LUMO}}{2} \quad [36, 37] \quad (4)$$
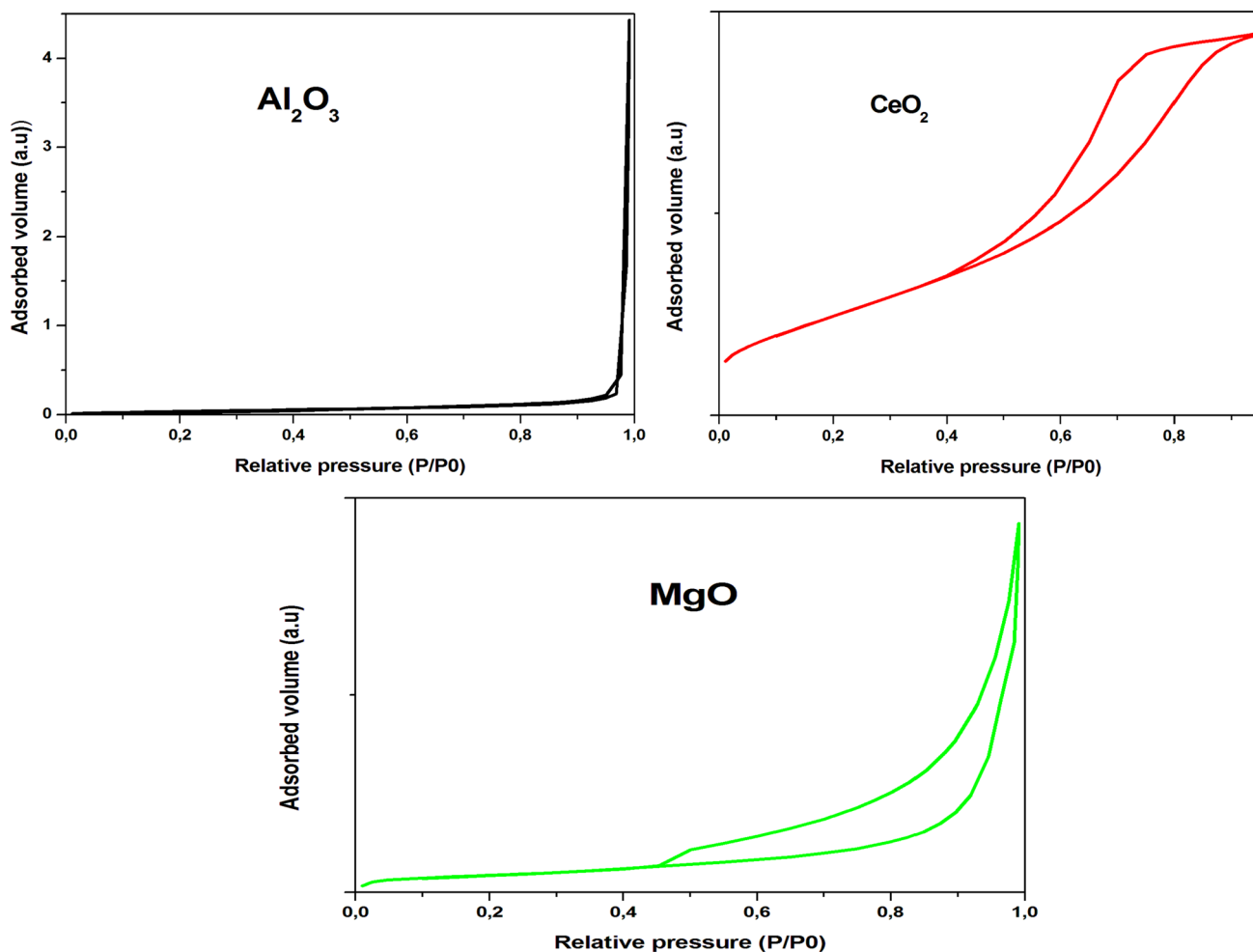
$$\eta = E_{LUMO} - E_{HOMO} \, [36, 38] \quad (5)$$

Fig. 3 N$_2$ adsorption–desorption isotherms of the oxide supports

$$S = 1/\eta \quad [36] \qquad (6)$$

Using the electronic chemical potential and chemical hardness definitions, the global electrophilicity index (ω), measures the stabilization of energy when the molecular system acquires an additional electronic charge from the environment, was then given by Parr [39] as

$$\omega = \mu^2/2\eta \qquad (7)$$

Therefore, the global nucleofilicity index (Nu) for a given system, was defined [40–42] as

$$N_u = E_{HOMO(Nu)} - E_{HOMO(TCE)} \qquad (8)$$

where EHOMO(Nu) is the HOMO energy of the nucleophile within the Kohn–Sham scheme [43, 44] and EHOMO(TCE) is the HOMO energy of the tetracyanoethylene (TCE) taken as reference, because it presents the lowest HOMO energy in a large series of molecules [40, 43].

3 Results and discussion

Table 2 shows the structural and textural characteristics of the studied materials. Cerium oxide and magnesium oxide are found to have comparable specific surfaces in order of 80 m^2.g^{-1}, whereas aluminum oxide has a very low surface of the order of 04 m^2.g^{-1}. There is also an increase in the surface area of the materials after doping with silver. This confirms the deposition of Ag in all catalysts. This can be linked to the participation of Ag (dopant nanoparticles) in the total area of the catalyst. Table 3 shows that practically all the silver has solution have been deposited on the surface of the support.

Figure 3 shows the N$_2$ adsorption–desorption isotherms of the oxide supports. According to the IUPAC classification, Al$_2$O$_3$ shows a type III isotherm which is generally obtained on nonporous or macroporous solids, for which the pore diameter is greater than 50 nm [45]. This is confirmed by the diameter obtained in our case by varying pore diameters from 116.52 nm (doped catalyst) to 88.11
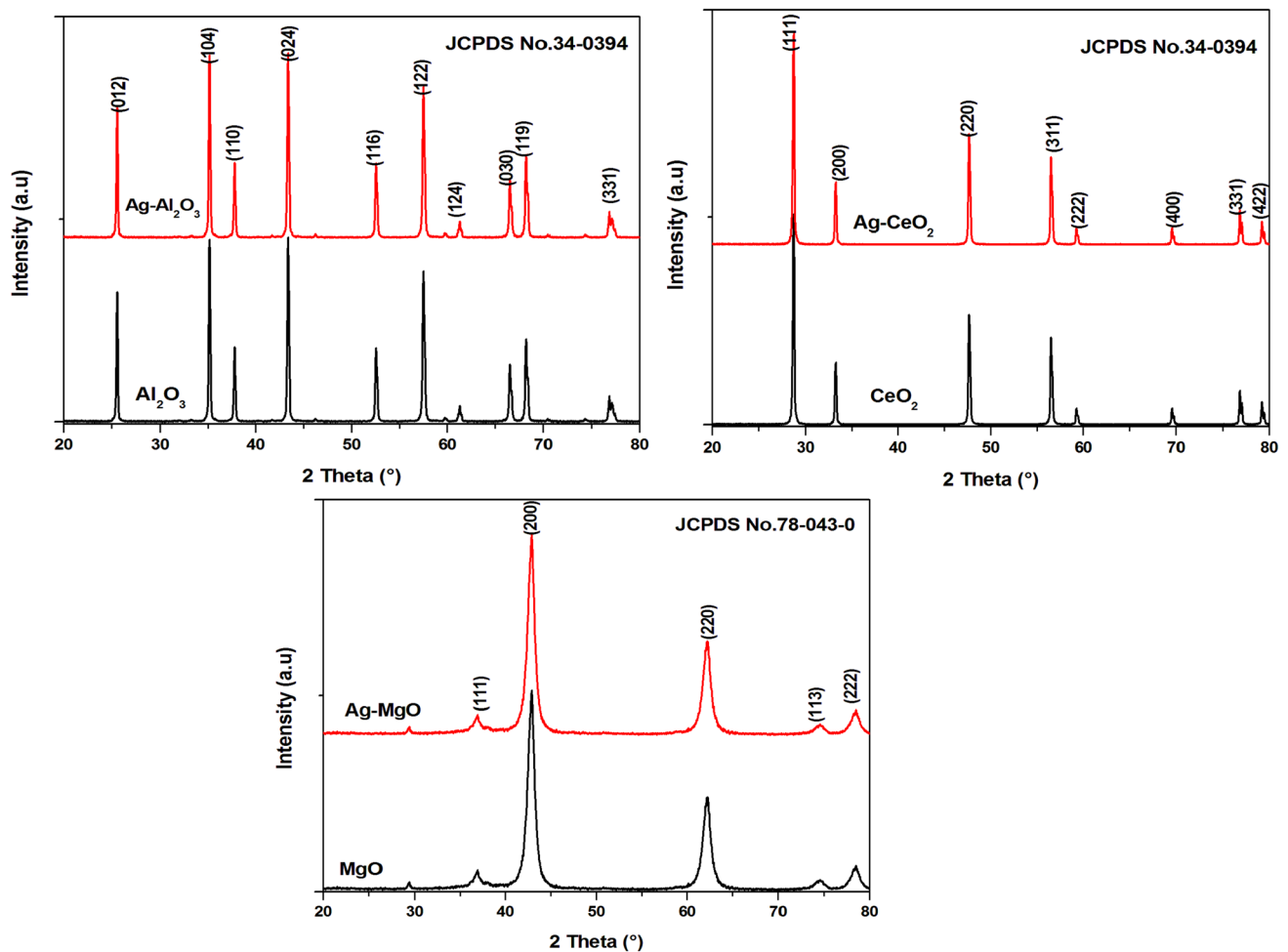
Fig. 4 XRD spectra of Al$_2$O$_2$, Ag–Al$_2$O$_3$, CeO$_2$, Ag–CeO$_2$, MgO and Ag–MgO materials, respectively

(undoped catalyst). However, MgO and CeO$_2$ exhibit a type IV adsorption–desorption isotherm that is obtained in the presence of mesoporous solids (2 nm ≤ diameter ≤ 50 nm). The jump appearing at high relative pressure values is related to the capillary condensation phenomenon (filling of mesoporosity). Once the pores are filled, adsorption continues on the surface of the solid. The reverse phenomenon takes place at a pressure different during desorption generating the hysteresis cycle [45]. However, the hysteresis loop is of the H2 type for CeO$_2$ linked to a so-called "ink bottle" pore shape or comes from an interconnected porosity consisting of pores of different shapes and sizes. The MgO has a hysteresis loop of the H3 type corresponding to slit pores of non-constant cross section [45]. In addition, we have obtained the same isothermal in the case of doped materials which induces that doping does not affect the properties of the supports. Finally, the doped materials have a slight improvement in the size of the pores which may be related to the incorporation of the silver nanoparticles in the pores.

XRD examination is performed in the range of 2θ = 20–80°. An XRD spectrum of the MgO is shown in Fig. 4. It visibly exhibits the rays at angles 36, 43, 63, 74 and 78° corresponds, respectively, to (1 1 1), (2 0 0), (2 2 0), (1 1 3), and (2 2 2) faces, which confirms the presence of pure polycrystalline cubic structure of MgO nanoparticles[46–48]. The mean crystallite size is calculated using the most intense peak (around 43°) and found to be 9.7 nm. The XRD spectrum of Al$_2$O$_3$ is also presented in Fig. 4 proving the presence of the alpha phase of alumina (α-Al$_2$O$_3$). The main peaks are confirmed at about: 25, 35, 37, 44, 53, 57, 60, 63, 67, 68 and 76° related, respectively, to the plans (012), (104), (110), (024), (116), (122), (124), (030), (119) and (331). The estimated average crystallite size is about 74 nm. The fluorite phase of cerium oxide nanoparticles is confirmed at 2 θ = 29° (1 1 1), 33° (2 0 0), 46° (2 2 0), 56° (3 1 1), 58° (2 2 2), 69° (4 0 0), 76° (3 3 1) and 79° (4 2 0).Finally, silver-doped materials do not show any characteristic lines to silver nanoparticles. This can be related to the
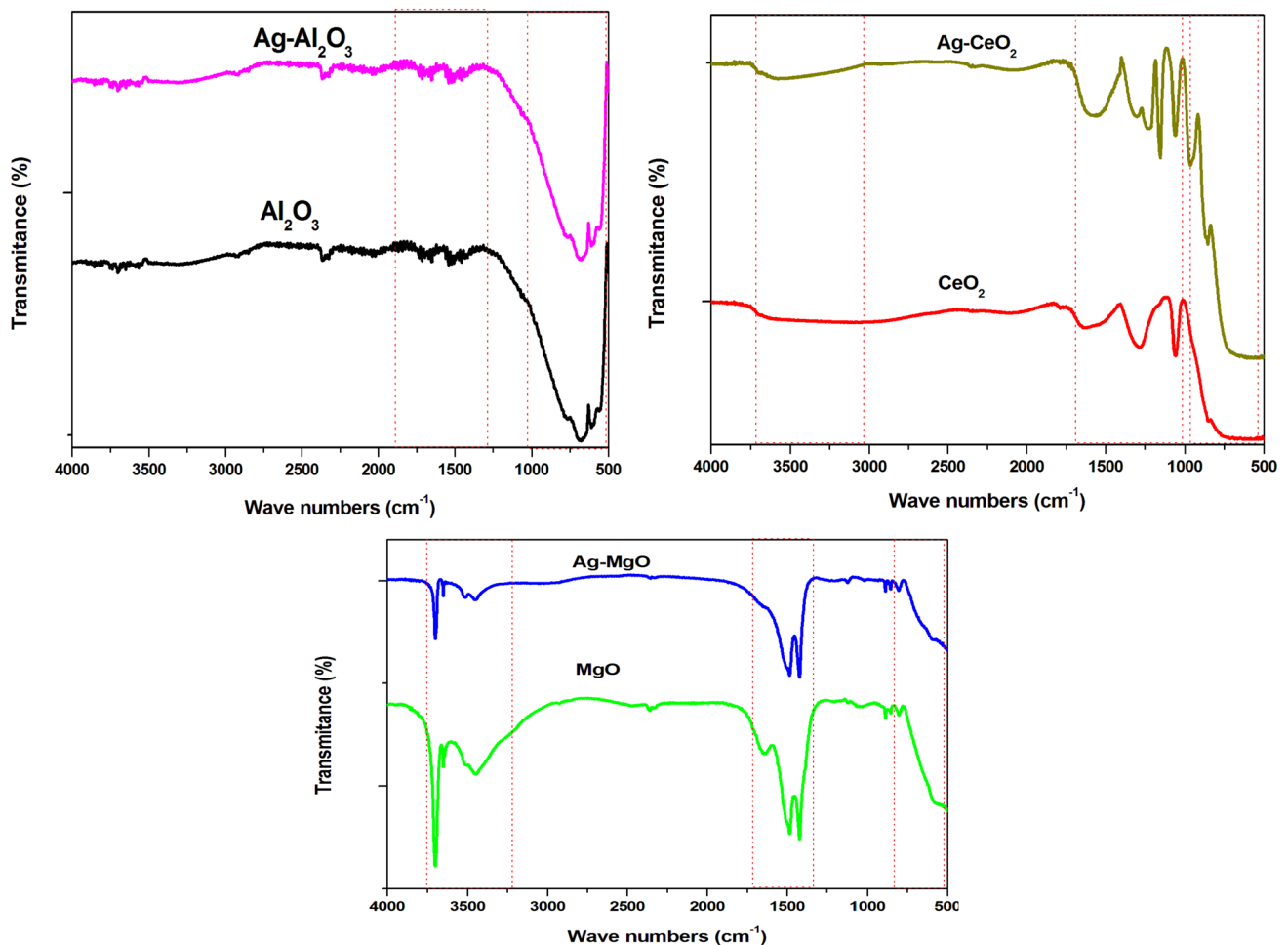
Fig. 5 FTIR spectra of Al_2O_2, Ag–Al_2O_3, CeO_2, Ag–CeO_2, MgO and Ag–MgO materials, respectively

low content of Ag (2 wt%) and the good distribution of metal particles on the surface of the supports [21, 49].

Figure 5 shows all the FTIR spectra of materials used in this study. Aluminum oxide has an intense band located around 600 cm^{-1}which is related to the stretching vibration of Al–O–H bond [50]. In the case of CeO_2, a broad band's located between 500 and 850 cm^{-1} are probably due to the Ce–O stretching vibrations [51]. FTIR spectrum of magnesium oxide (see Fig. 5) reveals the stretching vibration mode around 600–750 cm^{-1} suggesting Mg–O–Mg bonds [52, 53]. The literature evokes that MgO chemisorbs water moistures from the atmosphere due to its surface acid–base characteristics [54]. However, in all materials the bands in the region1200−1600 cm^{-1} and 3200–3600 cm^{-1}are due to hydroxyl group (O–H) stretching vibration mode of water absorbed from the humidity [47, 55].In the case of doped materials with silver nanoparticles, there is no change by contribution to the spectra of the supports except a slight shift or lowering of the intensity of the support bands. This

is explained by the metal support interaction and the establishment of certain link metal-support.

Figure 6 shows the Raman spectra of all samples. Raman spectroscopy was used to enrich the FTIR results and to search other phases not visible by FTIR method. This characterization technique has been practical as a surface, qualitative and non-destructive analytical method [56]. Raman spectroscopy of α-Al_2O_3 is presented in Fig. 6. Based upon a D^6_{3d} symmetry of corundum, six Raman active phonon modes, $2A_{1g}+4E_g$(optical and acoustical modes), at frequencies of 379 cm^{-1}, 412 cm^{-1}, 433 cm^{-1}, 570 cm^{-1}, 679 cm^{-1} and 766 cm^{-1} have been reported [57–59]. The Raman spectrum of CeO_2 support shown three peaks located at 249 cm^{-1}, 464 cm^{-1} and 613 cm^{-1}.The last two bands correspond, respectively, to the F_{2g} triply degenerate mode of fluorite created from the symmetric vibrations of oxygen atoms around the $Ce^{4+}$and to oxygen vacancies resulting from the Ce^{4+} reduction to Ce^{3+} ions [60]. It is worth noting that CeO_2 crystallizes in the cubic fluorite-type lattice and refers to the space group Fm3m. This arrangement have
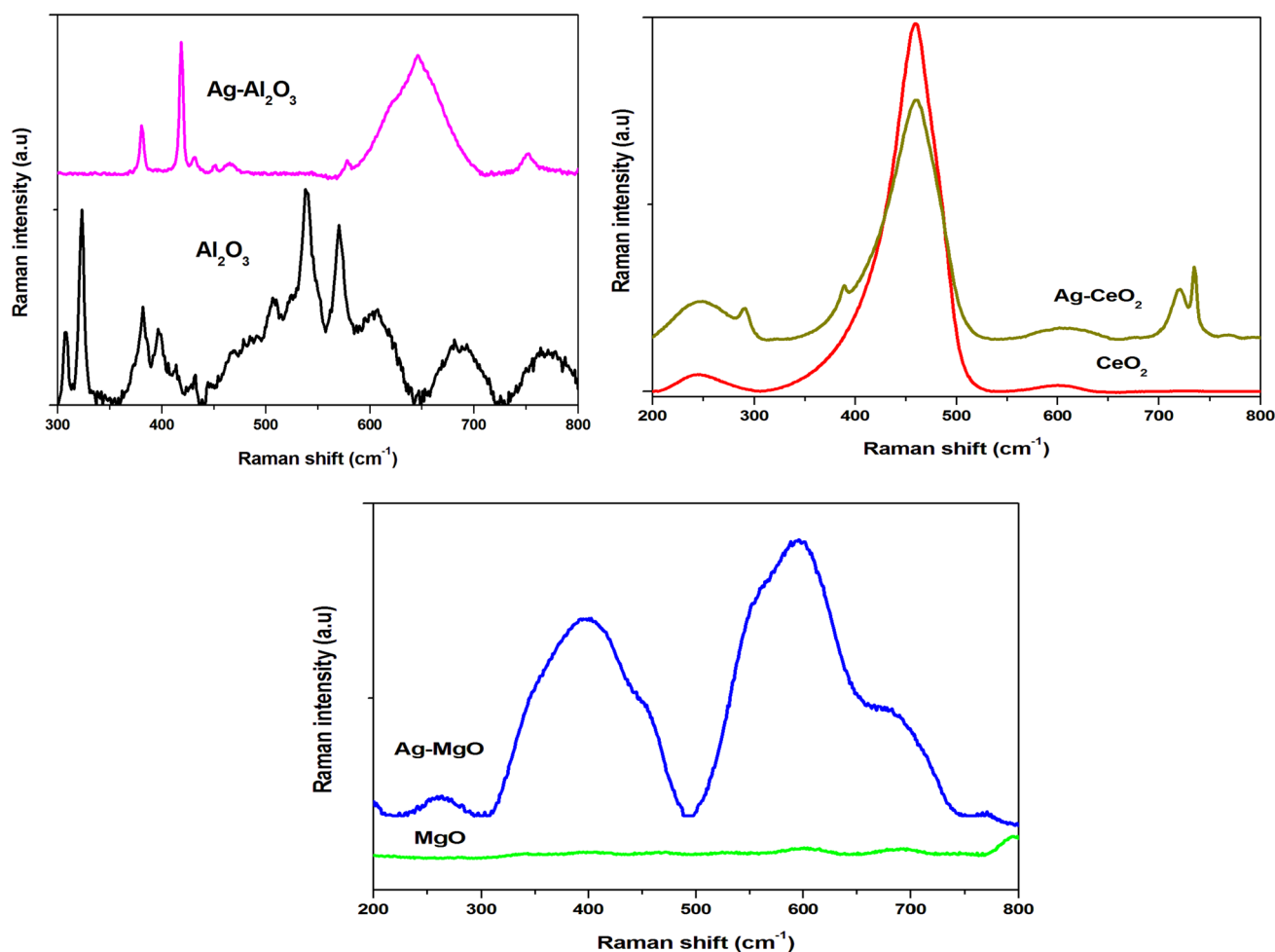
Fig. 6 Raman analysis of Al_2O_2, Ag–Al_2O_3, CeO_2, Ag–CeO_2, MgO and Ag–MgO materials, respectively

six optical-phonon branches, of which three of their located at the positions indicated above and are linked to the doubly degenerate transverse optical mode, the triply degenerate Raman-active and the nondegenerate longitudinal optical modes, respectively [61, 62]. In the case of MgO, the peaks at 280 cm^{-1} and 440 cm^{-1} are related to $Mg(OH)_2$ [60]. In the case of Ag-doped catalysts, the bands linked to the silver species can be clearly seen; especially in the case of the Ag–MgO catalyst. The metal species bands are clearly shown around 270, 430, 468, 580, 613 and 745 cm^{-1} related to the Ag_2O vibrational modes [56, 63, 64].

In summary, we can say that we have prepared catalysts based on silver nanoparticles supported on three different support oxides: Al_2O_3, CeO_2 and MgO. These supports have different characteristics: surface, crystallinity, particle size, acid–base character, oxidation–reduction character and others. However, Al_2O_3 is an insulator is excellent ceramic material having mechanical and optical properties. It is employed in advanced engineering applications, such

as: gas sensing compounds, dielectric materials, biomedical plans and automotive parts [57]. However, the catalytic reactions using ceria-based materials refer to the crucial characteristic which is the ease with which the Ce valence moves between Ce^{4+} and Ce^{3+}. The formation of a neutral oxygen vacancy is followed by the generation of a pair of Ce^{3+} ions [61]. Magnesia is a material of significant technological value. MgO is used in catalysis, treatment of toxic waste, paints additives, bactericides and adsorbents and others [65]. This is due to its high surface area and its important basic character [65]. Finally, silver nanoparticles possess important characteristics mainly due to their oxidation states, their size and their plasmon resonance band [3, 21, 56, 64, 66–68]. Doped on other supports (SiO_2, titanate nanotubes and Bentonite) these catalysts show surprising activities in the synthesis of heterocyclic derivatives molecules [2, 3]. Therefore, it would be interesting to use catalysts based on Ag nanoparticles supported on three different
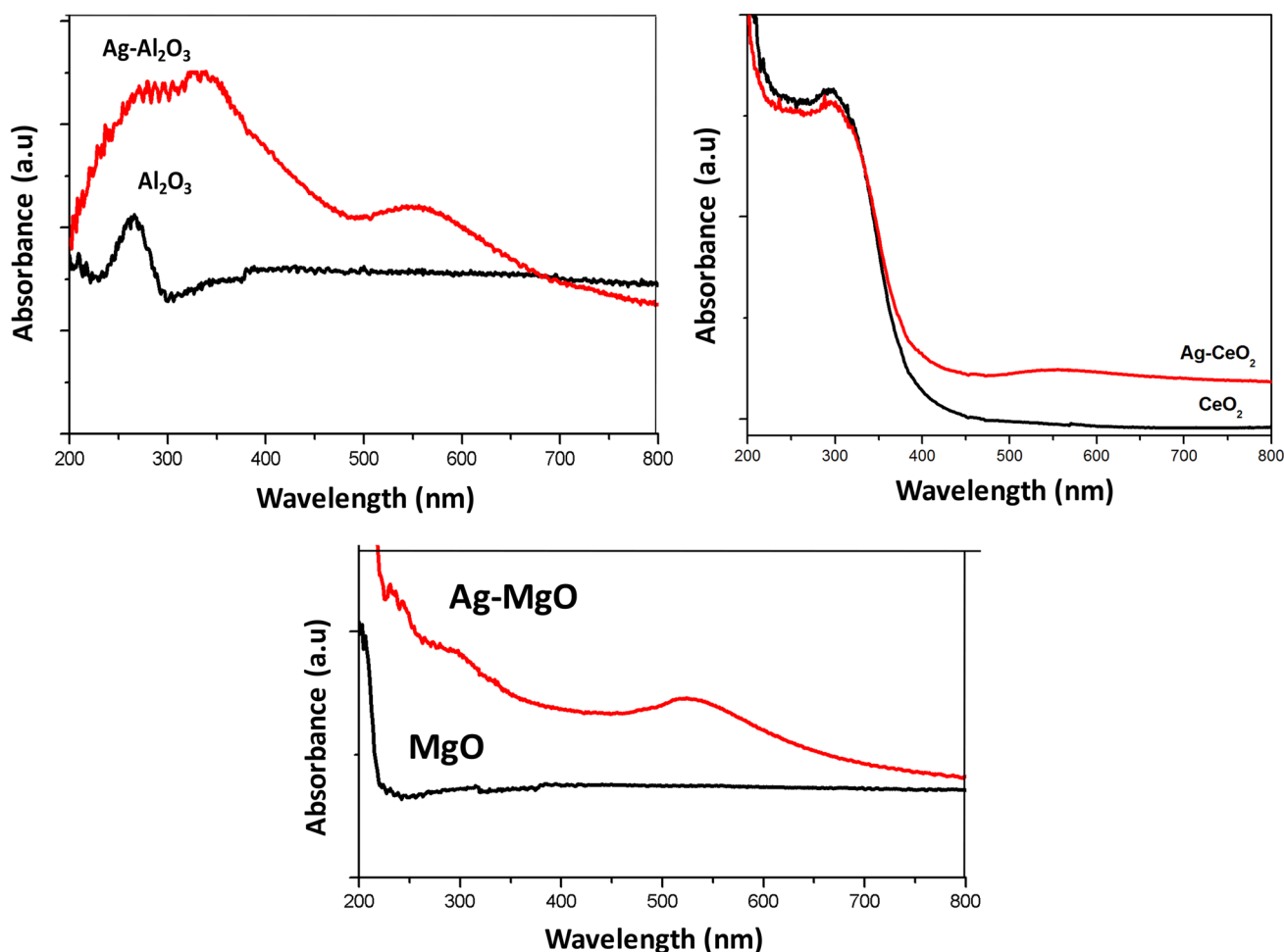
Fig. 7 UV–Vis spectra of Al_2O_2, Ag–Al_2O_3, CeO_2, Ag–CeO_2, MgO and Ag–MgO materials, respectively

oxides supports having different properties in the synthesis of heterocyclic molecules.

Figure 7 shows the UV–Vis spectra of the studied materials. It is clear that the Ag-doped catalysts all exhibit the plasmon resonance band characteristic of reduced silver nanoparticles (Ag^0 metal state) [69]. The clusters Agn ($1 < n < 10$) appear generally in the zone 387–453 nm. However, this band is influenced by the concentration, the temperature of the annealing treatment as well as the environment (the support) of the silver nanoparticles. A Babapour evoked that in the nano-silver silica films, the RSP appeared around in the range of 408 to 456 nm depending on the Ag concentration and the annealing temperature [70]. Where the SPR band in the case of Ag–Ce/TiO_2, metallic silver nanoparticles appeared in the region 516–547 nm [71]. In our case, the resonance band is between 500 and 550 nm depending on the nature of the support.

4 Application of the studied catalysts in the synthesis of heterocyclic molecules

The results of the 3-methyl-4-(4-(Dimethylamino) benzalidene)-isoxazole-5(4H)-one synthesis using water as solvent and with different catalysts for 24 h are presented in Table 3. The results show that the presence of the catalyst is important to advance the reaction. The presence of the catalysts leads to a remarkable increase in the yield compared with the addition to the blank reaction. Yields varying from 56% to 98% depending on the nature of the catalyst. It is important to note that the doped-materials showed the best yields and that undoped supports to a decrease of the order of 10% of catalytic activities. The best results are achieved with ceria-based catalysts; especially Ag–CeO_2, the yield obtained of achieved 98% (Table 3, entry 2). We can attribute this good activity to its large specific surface area, the nanometric size of these crystallites, the presence of Ce^{4+}/

Table 4 Results of the synthesis of 3-methyl-4-(1-phenyl-ethylidene)-isoxazole-5(4H)-one

| Catalysts	Solvents	Temperature (°C)	Yields (%)
CeO$_2$	Water	Ambient temperature	Trace
		70	
	EtOH	Ambient temperature	
		70	
	Water:EtOH (70:30)	Ambient temperature	
		70	
Lemon juice	Water	Ambient temperature	
		70	
	EtOH	Ambient temperature	
		70	
	Water:EtOH (70:30)	Ambient temperature	
		70	

Ce^{3+} species and the presence of silver nanoparticles. On the other hand, the low catalytic activity in the case of supports may be related to the low surface area of these materials (see Table 2), which leads to a decrease in the rate of active sites. However, the aim of this study is to prepare and test materials based on silver nanoparticles in the heterocyclic synthesis reaction respecting the rules of green chemistry. Silver nanoparticles have interesting activities which makes their application interesting. In addition, it is curious to see the fact that they are supported on support oxides having different natures. We have chosen three support oxides of different nature: MgO has a basic character, Al$_2$O$_3$ has properties as Lewis acid and CeO$_2$ which has an important red-ox character. We applied these materials in a model reaction that leads to the synthesis of 4-disubstituted isoxazol-5(4H)-ones which possess wide application. Yields varying between 64% and 98% were obtained, which can be attributed to the large surface area of the catalyst, the oxidation state of the silver nanoparticles and the nature of the support.

The reaction of 3-methyl-4-(1-phenylethylidene)-isoxazole-5(4H)-one was also carried out under various conditions (See Table 4), which led to negative results despite the change in color and the obtaining of two phases, which showed that the reaction did not exceed the intermediate state. In addition, research in the literature [20] evoked the synthesis of isoxazole-5(4 h)-one using lemon juice as excellent homogenous catalyst that gives important yields. This result inspired us to use it in the reaction in Fig. 8 but also negative results were obtained.

A possible mechanism (see Fig. 9) for the synthesis of 3,4-disubstituted isoxazol-5(4H)-one is proposed overall studied catalyst on the basis of the condensation of Knoevenagel reaction. In the beginning, the catalyst is coordinated with the oxygen of the carbonyl group of ethyl acetoacetate (step 1). Then, the free pair of nitrogen (in NH$_2$.OH) attacks the carbonyl carbon and the elimination of water is accrued (step 2). After, the intermediate results from the keto-enol tautomerism (step 3). In step 4, nucleophilic addition of aldehyde is linked with a catalyst to form intermediate. Consequently, the elimination of water molecules causes obtaining of an intermediate (step 5), which finally endure cycle close (or cyclization) to form the intermediate (Step 6) that eliminates the ethanol molecule to achieve the desired product and generates catalyst (Step 7) [2–7, 14–20, 72–74].

Figure 10 shows the stability of the Ag–CeO$_2$ catalyst during four successive cycles. A pronounced stability of the studied catalyst is observed; the same yield is completed during cycles. This can be a good indicator for a future application of ceria in this type of reaction in the industrial sector.
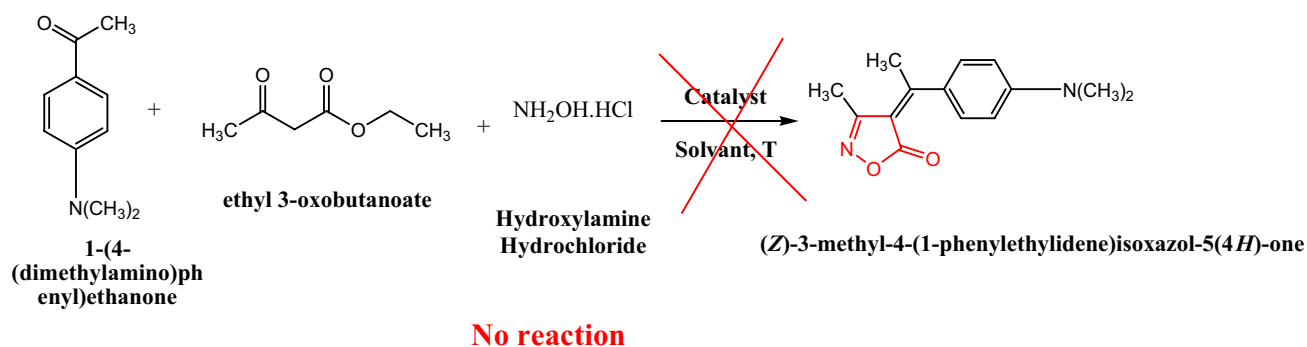
Fig. 8 Synthesis of 3,4-disubstituted isoxazol-5(4H)-ones using ketone as depart molecule
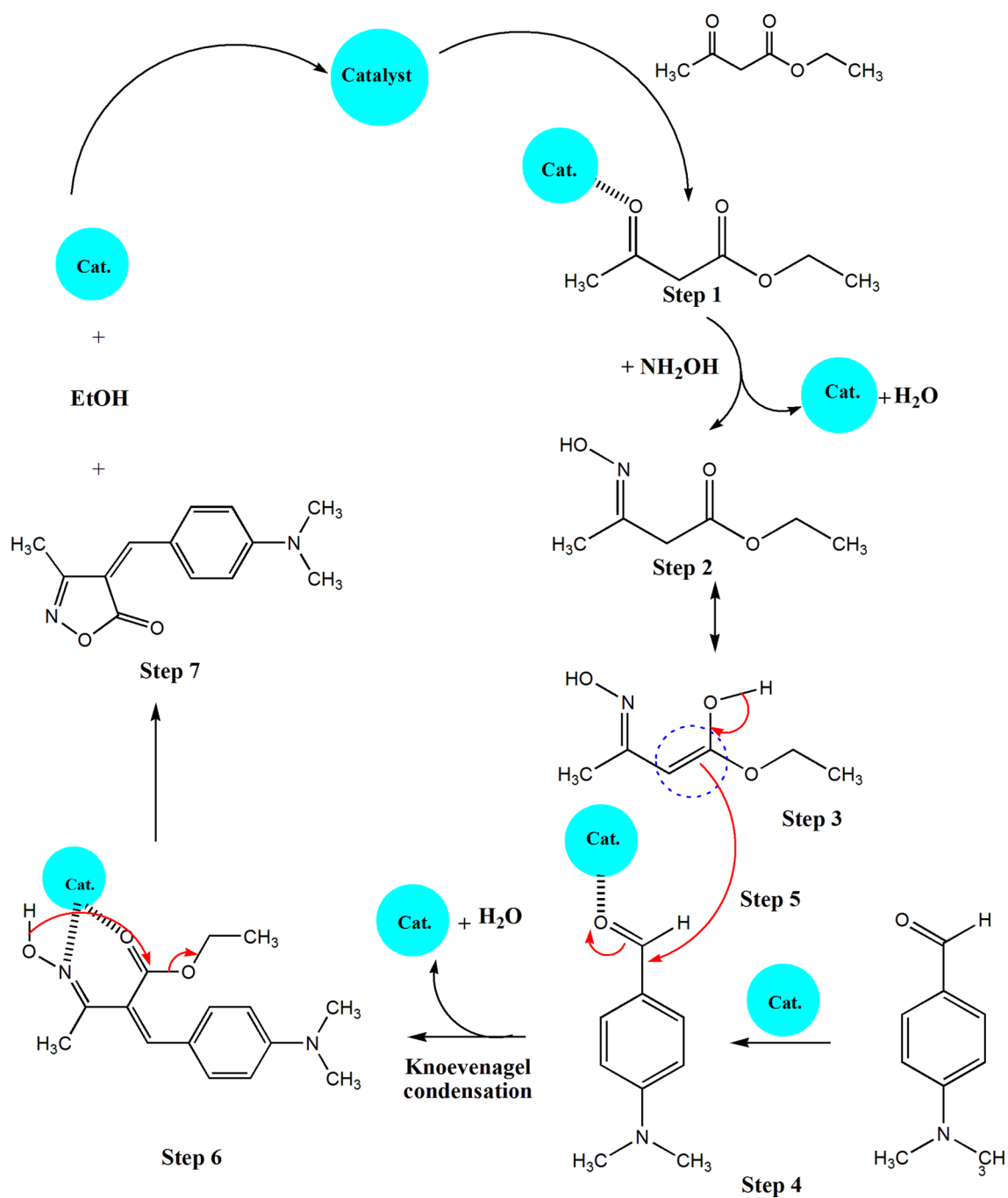
Fig. 9 Plausible mechanism for the synthesis of 3,4-disubstituted isoxazol-5(4H)-ones using catalysts
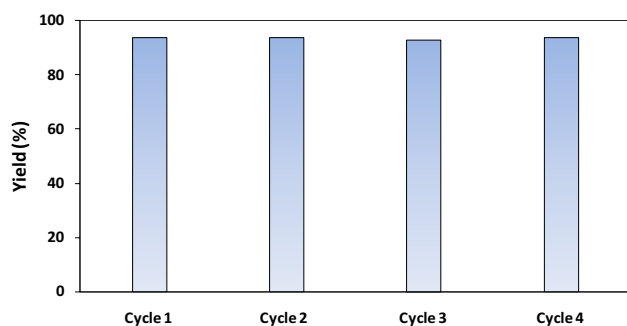
Fig. 10 Stability of Ag–CeO$_2$ catalyst during the synthesis of 3-methyl-4-(1-phenyl-ethylidene)-isoxazole-5(4H)-one

5 Properties of 3-methyl-4-(1-phenyl-ethylidene)-isoxazole-5(4H)-one: theoretical calculations

5.1 Geometric structure of 3-methyl-4-(1-phenyl-ethylidene)-isoxazole-5(4H)-one

For the 3-methyl-4-(1-phenyl-ethylidene)-isoxazole-5(4H)-one, geometry optimizations shown in Fig. 11 have been performed at B3LYP/6-31G(d) level and the calculated results are also listed in Table 5. Thus, the comparisons between the experiments [75] and the calculations can be more straightforward.

As shown in Tables 5 and 6, most of the predicted geometric parameters have higher values than those determined experimentally. This is most likely because that the experimental data describe the compounds in the solid state, whereas the calculated data correspond to the molecules in the gas phase. Comparing the predicted values with the

Fig. 11 Optimized geometry of 3-methyl-4-(1-phenyl-ethylidene)-isoxazole-5(4H)-one obtained at B3LYP/6-31G(d) theoretical level
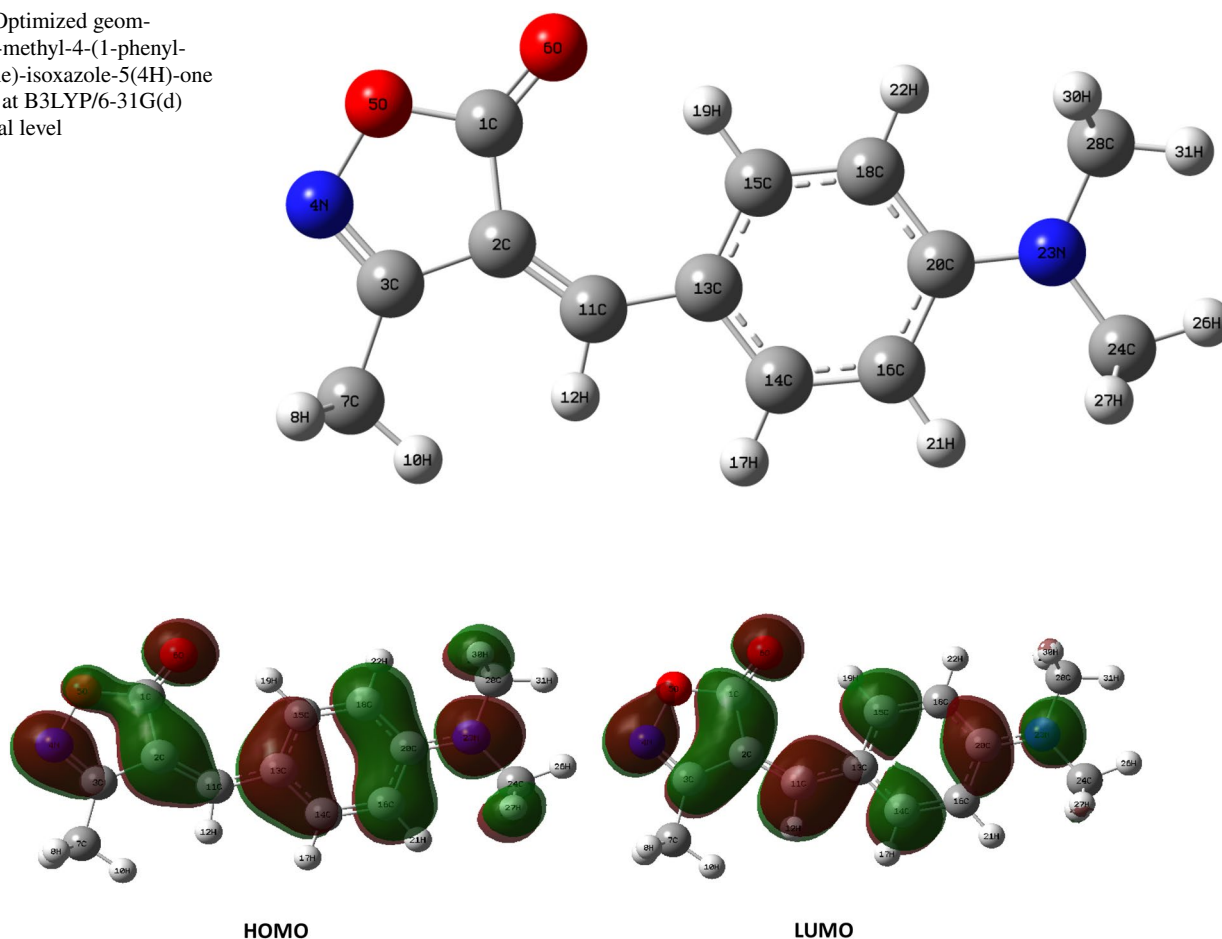

HOMO   LUMO

Fig. 12 Frontier molecular orbital representation of 3-methyl-4-(1-phenyl-ethylidene)-isoxazole-5(4H)-one

Table 5 Selected bond lengths (Å), bond angles (°) and torsion angles (°) determined by theoretical calculations at the DFT/B3LYP/6-31G(d)

Bond lengths (Å)	Cal	Exp.*	Bond lengths (Å)	Cal	Exp.*
O5–C1	1.3748	1.388 (4)	C3–N4	1.2968	1.294 (4)
O5–N4	1.4260	1.451 (3)	C3–C7	1.5040	1.481 (4)
C1–O6	1.2154	1.220 (4)	C11–C13	1.4376	1.426 (4)
C1–C2	1.4769	1.446 (5)	C20–N23	1.3721	1.367 (4)
C2–C3	1.4544	1.451 (4)	N23–C24	1.4554	1.457 (4)
C2–C11	1.3712	1.365 (5)	N23–C28	1.4565	1.455 (4)

Bond angles(°)	Cal	Exp.*	Bond angles(°)	Cal	Exp.*
C1–O5–N4	110.528	109.2 (3)	C2–C11–C13	134.336	135.0 (3)
O5–N4–C3	107.462	106.5 (3)	C2–C11–H12	113.521	112.5
N4–C3–C2	112.529	113.3 (3)	C11–C13–C14	117.350	117.8 (3)
C1–C2–C3	103.231	103.6 (3)	C11–C13–C15	125.916	125.4 (3)
O5–C1– C2	106.250	107.3 (3)	C16–C20–N23	121.311	120.8 (3)
O5–C1–O6	120.560	118.0 (3)	C18–C20–N23	121.408	122.0 (3)
C2–C3–C7	128.432	127.1 (3)	C20–N23–C24	120.246	120.9 (3)
C1–C2–C11	131.567	132.2 (3)	C20–N23–C28	120.271	121.9 (3)

Torsion angles(°)	Cal	Exp.*	Torsion angles(°)	Cal	Exp.*
O5–C1–C2–C3	− 0.010	− 0.9(4)	C3–C2–C11–C13	180.000	177.6 (3)
O5–C1–C2–C11	179.991	176.5 (4)	C2–C11–C13–C14	-179.999	− 179.7 (4)
C1–C2–C3–C7	− 179.996	− 178.2 (3)	C2–C11–C13–C15	0.000	− 0.4 (6)
C1–C2–C3–N4	0.006	0.3 (4)	C11–C13–C14–C16	− 180.000	− 179.8 (3)
O5–N4–C3–C2	0.000	0.4 (4)	C11–C13–C15–C18	− 180.000	− 179.5 (3)
O5–N4–C3–C7	179.998	178.9 (3)	C16–C20–N23–C24	− 0.014	− 4.7 (5)
C1–C2–C11–C13	0.002	0.8 (7)	C18–C20–N23–C28	− 179.979	− 179.2 (3)

*Ref [75]

experimental ones, it can be found that the biggest difference in bond length occurs at bond C1–C2 with the difference being 0.0304 Å. Considering the bond angles, the biggest variation between the experimental and predicted values can be found at bond angle O5–C1–O6 with the difference being 2.53°.

Furthermore, the most important difference established for torsion angles is at the C16–C20–N23–C24 with a value of 4.736°. Comparisons indicate that, while there exist some differences of the geometrical parameters between the experiments and the predictions, the optimized geometry resembles directly their crystal structures [75] and

B3LYP/6-31G(d) level of theory can give agreeable calculation precision for the studied molecule.

6 Frontier orbitals analysis and related molecular properties

The electronic frontier orbitals are responsible for chemical reactivity and stability of the desired molecular system [76–78]. Parr and Yang demonstrated that most of the electron frontier theory of chemical reactivity can be derived from DFT [79]. The highest occupied molecular orbital

Table 6 *HOMO* and *LUMO* energies, energy *gap*, electronic chemical potential μ, chemical hardness η, global electrophilicity ω and global nucleophilicity N_u

HOMO (au)	LUMO (au)	E_{GAP} (au)	μ (au)	η (au)	ω (eV)	N_u^a (eV)
− 0.20135	− 0.08060	0.12075	− 0.140975	0.12075	2,03,197	3,6,395,515

(HOMO) and the lowest unoccupied molecular orbital (LUMO) for the complex are shown in Fig. 12.

[a]The HOMO energy of the reference system tetracyanoethylene is – 0.3351 eV calculated at the same level of theory.

The HOMO energy is habitually related to the electron-donating ability of a molecule; that high energy values of HOMO are likely to designate a tendency of the molecule to donate-electrons [80]. The LUMO energy is associated to the electron affinity [29]. The molecule having the higher energy gap is more stable, less reactive and is also termed as hard molecule and vice versa[81].The negative values of HOMO energy and chemical potential showed that the 3-methyl-4-(1-phenyl-ethylidene)-isoxazole-5(4H)-one under study is a stable compound (see Table 6).

7 Conclusions

The aim of the present study was to produce catalysts based on silver nanoparticles supported on three supports of different nature: CeO_2, Al_2O_3 and MgO. The results of the characterizations showed the obtaining of catalysts having different surfaces but the Ag–CeO_2 catalysts has the best surface. In addition, the results of the RD/UV–Vis analysis revealed that the nanoparticles are in their metallic state "Ag^0".For the synthesis of 3-methyl-4-(1-phenyl-ethylidene)-isoxazole-5(4H)-one, yields varying between 64% and 94% were obtained depending on the nature of the catalyst. However, the catalysts Ag–CeO_2 showed the best catalytic activity which may be related to the best catalyst surface and the presence of silver nanoparticles. Finally, we performed for the first time DFT calculations to mount the geometry, structure and properties of the 3-methyl-4-(1-phenyl-ethylidene)-isoxazole-5(4H)-one.

References

1. N. Ergenç, G. Çapan, G. Ötük, Pharmazie **48**, 780–782 (1993)
2. S.N. Maddila, S. Maddila, W.E. van Zyl, S.B. Jonnalagadda, Res. Chem. Intermed. **42**, 2553–2566 (2016)
3. N. Ameur, G. Ferouani, Z. Belkadi, R. Bachir, J.J. Calvino, A. Hakkoum, Mater. Res. Express **6**, 125051 (2019)
4. G. Ferouani, N. Ameur, R. Bachir, Res. Chem. Intermed. **46**, 1373–1387 (2020)
5. H. Kiyani, F. Ghorbani, J. Saudi Chem. Soc. **21**, S112–S119 (2017)
6. S.K. Asadi, G. Aleaba, N. Daneshvar, F. Shirini, Sustainable Chem. Pharm. **21**, 100442 (2021)
7. S.A. Pourmousavi, H.R. Fattahi, F. Ghorbani, A. Kanaani, D. Ajloo, J. Iran. Chem. Soc. **15**, 455–469 (2018)
8. A. Muthuvel, M. Jothibas, C. Manoharan, J. Environ. Chem. Eng. **8**, 103705 (2020)
9. A. Muthuvel, M. Jothibas, C. Manoharan, Nanotechnol. Environ. Eng. **5**, 14 (2020)
10. N. Al-Zaqri, K. Umamakeshvari, V. Mohana, A. Muthuvel, A. Boshaala, J. Mater. Sci. **33**, 11864–11880 (2022)
11. A. Muthuvel, N.M. Said, M. Jothibas, K. Gurushankar, V. Mohana, J. Mater. Sci. **32**, 23522–23539 (2021)
12. J. Vasudevan, S. Johnson Jeyakumar, B. Arunkumar, M. Jothibas, A. Muthuvel, S. Vijayalakshmi, Mater. Today: Proc., 48 :438–442 (2022)
13. S.N. Maddila, S. Maddila, W.E. van Zyl, S.B. Jonnalagadda, RSC Adv. **5**, 37360–37366 (2015)
14. M. Shanshak, S. Budagumpi, J.G. Małecki, R.S. Keri, Appl. Organomet. Chem. **34**, e5544 (2020)
15. H. Kiyani, H.A. Samimi, Chiang Mai J. Sci. **44**, 1011–1021 (2017)
16. F. Ghorbani, H. Kiyani, S.A. Pourmousavi, Res. Chem. Intermed. **46**, 943–959 (2020)
17. H.R. Saadati-Moshtaghin, B. Maleki, R. Tayebee, S. Kahrobaei, F. Abbasinohoji, Polycyclic Aromat. Compd., (2020) 1–12
18. A.B. Barkule, Y.U. Gadkari, V.N. Telvekar, Polycyclic Aromat. Compd., (2021) 1–12
19. Q. Liu, X. Hou, Phosphorus Sulfur Silicon Relat. Elem. **187**, 448–453 (2012)
20. R.H. Vekariya, K.D. Patel, H.D. Patel, Res. Chem. Intermed. **42**, 7559–7579 (2016)
21. L. Zhang, C. Zhang, H. He, J. Catal. **261**, 101–109 (2009)
22. Q. Chang, L. Yan, M. Chen, H. He, J. Qu, Langmuir **23**, 11197–11199 (2007)
23. R.G. Parr, Density functional theory of atoms and molecules, in: Horizons of quantum chemistry, Springer, 5–15 (1980)
24. P. Hohenberg, W. Kohn, Phys. Rev. **136**, B864 (1964)
25. R. Dreizler, E. Gross, Density Functional Theory Springer Verlag, in, Berlin New York, 1990
26. R.G. Parr, W. Yang, Annu. Rev. Phys. Chem. **46**, 701–728 (1995)
27. W. Kohn, A.D. Becke, R.G. Parr, J. Phys. Chem. **100**, 12974–12980 (1996)
28. H. Chermette, J. Comput. Chem. **20**, 129–154 (1999)
29. P. Geerlings, F. De Proft, W. Langenaeker, Chem. rev. **103**, 1793–1874 (2003)
30. W. Kohn, L.J. Sham, Phys.rev., 140, A1133 (1965)
31. M. Frisch, G. Trucks, H.B. Schlegel, G.E. Scuseria, M.A. Robb, J.R. Cheeseman, G. Scalmani, V. Barone, B. Mennucci, G. Petersson, Inc., Wallingford CT, 201 (2009)
32. A.N. Mayeno, J.L. Robinson, R.S. Yang, B. Reisfeld, J. Chem. Inf. Model. **49**, 1692–1703 (2009)
33. A.D. Becke, J. Chem. Phys. **96**, 2155–2160 (1992)
34. P.J. Stephens, F.J. Devlin, C.F. Chabalowski, M.J. Frisch, J. Chem. Phys. **98**, 11623–11627 (1994)
35. C. Lee, W. Yang, R.G. Parr, Phys. rev. B **37**, 785 (1988)
36. R. Parr, W. Yang, Press, New York, (1989)
37. R.G. Parr, R.A. Donnelly, M. Levy, W.E. Palke, J. Chem. Phys. **68**, 3801–3807 (1978)
38. R.G. Parr, R.G. Pearson, J. Am. Chem. Soc **105**, 7512–7516 (1983)
39. R.G. Parr, L.v. Szentpály, S. Liu, J. Am. Chem. Soc, 121,1922–1924 (1999)
40. L.R. Domingo, E. Chamorro, P. Pérez, J. org. chem. **73**, 4615–4624 (2008)
41. L.R. Domingo, E. Chamorro, P. Perez, J. Chem. Phys. A **112**, 4046–4053 (2008)
42. L.R. Domingo, P. Pérez, Org. Biomol. Chem. **9**, 7168–7175 (2011)

43. P. Jaramillo, L.R. Domingo, E. Chamorro, P. Pérez, J. Mol. Struct.: THEOCHEM **865**, 68–72 (2008)
44. H.B. Schlegel, J. Comput. Chem. **3**, 214–218 (1982)
45. W.S. KS, D. Everett, W. RA, L. Haul, Pure Appl. Chem, 57,603–619 (1985)
46. G. Balakrishnan, R. Velavan, K. Mujasam Batoo, E.H. Raslan, Results Phys., 16,103013 (2020)
47. N.M. El-Sawy, A.I. Raafat, N.A. Badawy, A.M. Mohamed, Int. J. Biol. Macromol. **142**, 254–264 (2020)
48. B. Yalagala, S. Khandelwal, D. J, S. Badhulika, Mater. Sci. Semicond. Process., 104,104673 (2019)
49. M.-F. Luo, P. Fang, M. He, Y.-L. Xie, J. Mol. Catal. A: Chem. **239**, 243–248 (2005)
50. L. Favaro, A. Boumaza, P. Roy, J. Lédion, G. Sattonnay, J.B. Brubach, A.M. Huntz, R. Tétot, J. Solid State Chem. **183**, 901–908 (2010)
51. G. Jayakumar, A.A. Irudayaraj, A.D. Raj, Mechanics, Mater. Sci. Eng. 9 (2017)
52. H. Niu, Q. Yang, K. Tang, Y. Xie, J. Nanopart. Res. **8**, 881–888 (2006)
53. A.M.B. Silva, C.M. Queiroz, S. Agathopoulos, R.N. Correia, M.H.V. Fernandes, J.M. Oliveira, J. Mol. Struct. **986**, 16–21 (2011)
54. K. Mageshwari, S.S. Mali, R. Sathyamoorthy, P.S. Patil, Powder Technol. **249**, 456–462 (2013)
55. F. Gu, S.F. Wang, M.K. Lü, W.G. Zou, G.J. Zhou, D. Xu, D.R. Yuan, J. Cryst. Growth **260**, 507–510 (2004)
56. I. Martina, R. Wiesinger, D. Jembrih-Simbürger, M. Schreiner, E-Preserv Sci **9**, 1–8 (2012)
57. P.G. Li, M. Lei, W.H. Tang, Mater. Lett. **64**, 161–163 (2010)
58. Y. Chen, J. Hyldtoft, C.J.H. Jacobsen, O.F. Nielsen, Spectrochim. Acta, Part A **51**, 2161–2169 (1995)
59. R. Krishnan, R. Kesavamoorthy, S. Dash, A.K. Tyagi, B. Raj, Scr. Mater. **48**, 1099–1104 (2003)
60. K. Aggoun, L. Chaal, J. Creus, R. Sabot, B. Saidani, M. Jeannin, Surf. Coat. Technol. **372**, 410–421 (2019)
61. C. Schilling, A. Hofmann, C. Hess, M.V. Ganduglia-Pirovano, J. Phys. Chem. C **121**, 20834–20849 (2017)
62. B.M. Reddy, A. Khan, Y. Yamada, T. Kobayashi, S. Loridant, J.-C. Volta, J. Phys. Chem. B **107**, 5162–5167 (2003)
63. C. Li, C. Yang, S. Xu, C. Zhang, Z. Li, X. Liu, S. Jiang, Y. Huo, A. Liu, B. Man, J. Alloys Compd. **695**, 1677–1684 (2017)
64. Z. Li, M. Wang, Y. Jiao, A. Liu, S. Wang, C. Zhang, C. Yang, Y. Xu, C. Li, B. Man, Sens. Actuators, B, 255,374–383 (2018)
65. D.C. Prado, I. Fernández, J.E. Rodríguez-Páez, Nano-Struct. Nano-Objects **23**, 100482 (2020)
66. X. Li, J. Li, X. Zhou, Y. Ma, Z. Zheng, X. Duan, Y. Qu, Carbon **66**, 713–719 (2014)
67. M. Lippits, A. Gluhoi, B. Nieuwenhuys, Top. Catal. **44**, 159–165 (2007)
68. K.G. Stamplecoskie, J.C. Scaiano, V.S. Tiwari, H. Anis, J. Phys. Chem. C **115**, 1403–1409 (2011)
69. J.C. Durán-Álvarez, E. Avella, R.M. Ramírez-Zamora, R. Zanella, Catal. Today **266**, 175–187 (2016)
70. A. Babapour, O. Akhavan, R. Azimirad, A. Moshfegh, Nanotechnology **17**, 763 (2006)
71. H. Chaker, S. Fourmentin, L. Chérif-Aouali, ChemistrySelect **5**, 11787–11796 (2020)
72. M. Parveen, A. Aslam, A. Ahmad, M. Alam, M.R. Silva, P.S.P. Silva, J. Mol. Struct. **1200**, 127067 (2020)
73. G.H. Oliveira, L.M. Ramos, R.K. de Paiva, S.T. Passos, M.M. Simões, F. Machado, J.R. Correa, B.A. Neto, Org. Biomol. Chem. **19**, 1514–1531 (2021)
74. D. Tang, Z. Iqbal, J. Sun, J. Ji, M. Yang, Z. Yang, Tetrahedron Lett. **62**, 152685 (2021)
75. Q. Cheng, Q.-f. Wang, L.-s. Liu, J.-l. Zhang, Acta Crystallogr., Sect. E: Struct. Rep. Online, 65,o3074-o3074 (2009)
76. K. Fukui, science, 218,747–754 (1982)
77. A.E. Reed, R.B. Weinstock, F. Weinhold, J. Phys. Chem. **83**, 735–746 (1985)
78. K. Fukui, T. Yonezawa, H. Shingu, J. Phys. Chem. **20**, 722–725 (1952)
79. R.G. Parr, W. Yang, J. Am. Chem. Soc. **106**, 4049–4050 (1984)
80. A.Y. Musa, A.A.H. Kadhum, A.B. Mohamad, A.A.B. Rahoma, H. Mesmari, J. Mol. Struct. **969**, 233–237 (2010)
81. G. Gece, S. Bilgiç, Corros. Sci. **51**, 1876–1878 (2009)